Appendix-12 Measurement results of sulfur isotopic composition.

No.	Sample No.	District	Locality	Type	$\delta^{34}S$ (‰)
1	A00MZ012	Andacollo	Mina Sofia, Level1	Pyrite in quartz vein	+3.5
2	A00MZ014	Andacollo	Mina Sofia	Pyrite in black mudstone	-14.9
3	A00MZ029	Mina Maria	Mina Maria	Galena vein	-0.3
4	A00MZ036	Condorcanqui	Condorcanqui	Chalcopyrite in andesite	-26.7
5	A00MZ042	Huemules	Huemules Sur	Galena vein	-1.8
6	A00MZ060	Arroyo Cascada	Arroyo Cascada	Pyrite in quartz vein	+6.6
7	A00MZ066	Ferrocarrilera	Ferrocarrilera	Pyrite in quartz vein	-0.4
8	A00MZ131	Condorcanqui	Condorcanqui	Chalcopyrite dissemination	+1.9
9	A00MZ135	Condorcanqui	Condorcanqui	Chalcopyrite in amygdale part	+4.1
10	A00MZ136	Condorcanqui	Condorcanqui	Andesite	+11.4
11	A00MZ137	Condorcanqui	North of Epuyen town	Granodiorite	+11.1

Appendix-13 Measurement results of oxygen isotopic composition.

No.	Sample	District	Locality	Type	T(°C) Max	T(°C) Min	T(°C) Average	NaCl(%) Average	$\delta 18O$ (‰) qz	$\delta 18O$ (‰) qz-water	$\delta 18O$ (‰) water
1	A00MZ012	Andacollo	Mina Sofia, Level1	Quartz-sulfides vein	235	193	214	3.6	11.2	10.8	0.4
2	A00MZ043	Huemules	Huemules Sur	Quartz-sulfides veinlet	144	109	130	1.8	9.2	17.3	-8.1
3	A00MZ046	Huemules	Huemules Sur	Quartz-sulfides veinlet	141	105	121	2.2	8.5	18.2	-9.7
4	A00MZ048	Joya del Sol	Brancote-Elena Sur	Qz vein	153	108	131	1.4	7.5	17.2	-9.7
5	A00MZ051	Joya del Sol	Brancote-Galadriel	Qz vein	173	121	147	0.7	4.1	15.6	-11.5
6	A00MZ066	Ferrocarrilera	Ferrocarrilera	Quartz-sulfides vein	223	177	204	2.5	10.3	11.4	-1.1
7	A00TM039	Cushamen	Cushamen	Qz vein	283	215	259	29.6	9.7	8.5	1.2
8	A00TM042	Cerro Gonzalo	Cerro Gonzalo	Qz vein	295	241	274	3.7	10.7	7.9	2.8
9	A00TM059	Estrella Gaucha	Estrella Gaucha	Qz vein	151	119	136	1.2	7.3	16.7	-9.4
10	A00MZ119	Arroyo Cascada	Arroyo Cascada	Qz vein	238	189	219	1.4	11.3	10.5	0.8
11	A00MZ148	Epuyen	Epuyen lake side	Qz vein	242	195	218	1	11.7	10.5	1.2

Appendix-14 K-Ar radiometric measurement results.

No.	sample No.	material	Isotopic Age(Ma)	$Ar^{40}scc/g \times 10^{-5}$	$\%Ar^{40}$	%K
1	A00NK050	Whole rock	119.0±6.0			
				0.743	84.5	1.58
				0.768	86.2	1.58
2	A00TM009	Plagioclase	53.8±3.0			
				0.145	37.3	0.66
				0.135	36.3	0.66
3	A00TM020	Plagioclase	64.7±3.2			
				0.185	54.2	0.74
				0.194	47.3	0.74
4	A00MZ108	Whole Rock	77.0±3.9			
				0.611	93.3	2.01
				0.619	93.8	2.01
5	A00MZ130	Whole Rock	108±5			
				0.741	94.2	1.71
				0.743	93.5	1.72
6	A00MZ139	Whole Rock	28.1±1.4			
				0.110	71.4	0.98
				0.106	76.5	0.98
7	A00TM125	Hornblende	13.2±0.7			
				0.077	62.4	1.51
				0.079	65.1	1.52
8	A00TM151	Biotite	65.0±3.3			
				0.478	85.9	1.79
				0.446	89.1	1.80

by Teledyne environmental service

Appendix – 15

Basic knowledge on stable isotopes and rare earth elements

1. Sulfur isotope

Sulfur isotopic composition concerning $^{34}S/^{32}S$ is defined as following formula, and standard material is troilite of Canyon Diablo meteorite (CDT).

$$\delta^{34}S(\text{‰}) = \left(\frac{Rx}{Rs} - 1\right) \times 1000 \qquad R = {^{34}S}/{^{32}S}, x = sample, s = s\tan dard.$$

It is known that the sulfur isotopic compositions of igneous rocks are relatively close to 0‰ of the standard and show a narrow variation range. Sasaki and Ishihara (1979) clarified that Japanese granite of the magnetite series range from 0 to +9‰. On the other hand, it is known that the sulfur isotopic compositions in sedimentary rocks show a wide variation range due to the isotopic fractionation effect by bacteria. Based on the knowledge, origin of sulfur for mineralization can be interpreted by measured isotopic compositions. For example, sulfides of the Bingham porphyry Cu deposit in USA indicate −3.11‰ to +3.87‰, and it means that sulfur originated from deep seated source within mantle (Field, 1966). Concerning the Shakanai kuroko deposit in Japan, sulfides indicate +5‰ to +8‰ coincident with magnetite series granitoids, and sulfates indicate +22‰ to +24‰ coincident with Tertiary evaporates (Sakai and Matsuhisa, 1996).

However, sulfur isotopic geochemistry is not simple in case that different sulfur species are coexisting, such as H_2S and SO_4^{2-}. As shown in Fig. 1, isotopic composition is variable, and isotopic fractionation that is difference of isotopic compositions between different sulfur species is depending on the temperature (Rye and Ohomoto, 1974). Therefore, it must be understood that the measured isotopic composition of sulfur compound is not always same as the isotopic composition of ore forming fluid.

For example of the isotopic fractionation, a case study for the Nansatsu high sulfidation Au deposits in Japan (Hedenquist et al., 1994) is quoted as follows.

In these deposits, hypogene alunite samples have values ranging from +24.5‰ to +34‰, and differences between hypogene alunite and sulfides are 28‰ to 25‰. In this case, 200 ℃ to 240℃ is estimated based on the isotopic fractionation shown in Fig. 1. Moreover, assuming the total Sulfur isotopic composition is +5‰ from fresh magnetite series intrusives, the sulfide/sulfate ratio of the original fluid can be calculated. X as the sulfur isotopic composition of sulfide and Y as that of
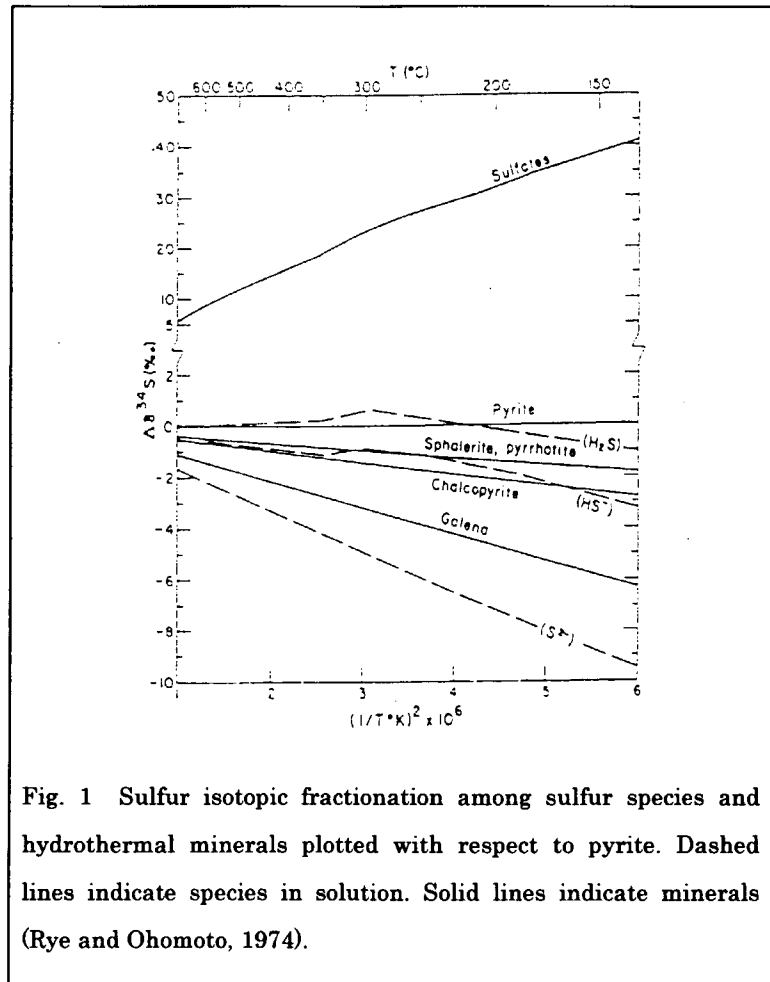

Fig. 1 Sulfur isotopic fractionation among sulfur species and hydrothermal minerals plotted with respect to pyrite. Dashed lines indicate species in solution. Solid lines indicate minerals (Rye and Ohomoto, 1974).

sulfate, the relation of "aY + (1 - a) X = 5‰" is established. Then 0.25 is calculated for "a" from Y = +26‰ and X = -2‰, and it means that sulfide/sulfate ration is 0.75 : 0.25 (Hedenquist et al., 1994).

2. Oxygen isotope

Oxygen isotopic composition concerning $^{18}O/^{16}O$ is defined as following formula, and standard material is Standard Mean Oceanic Water (SMOW).

$$\delta^{18}O(‰) = \left(\frac{Rx}{Rs} - 1\right) \times 1000 \qquad R = {}^{18}O/{}^{16}O, x = sample, s = s\tan dard.$$

Oxygen isotopic composition of hydrothermal water can be calculated based on the measured oxygen isotopic composition and homogenization temperature of fluid inclusions for the hydrothermal product, such as quartz and calcite, according to the following formulas. The isotopic fractionation factors for other minerals are reported by Kieffer (1982) and Field and Fifarek (1985) etc.

$$10^3 \ln\alpha = \delta\ ^{18}O_{quartz} - \delta\ ^{18}O_{water} = \frac{3.34 \times 10^6}{T^2} - 3.31 \quad (\textit{Matsuhisa et al.,1979})$$

$10^3 \ln\alpha$ = isotopic fractionation factor
T = abosolute temperature, Range = 250 to 500 ℃

$$10^3 \ln\alpha = \delta\ ^{18}O_{calcite} - \delta\ ^{18}O_{water} = \frac{2.78 \times 10^6}{T^2} - 2.89 \quad (\textit{Friedman and O'Neil,1977})$$

$10^3 \ln\alpha$ = isotopic fractionation factor
T = abosolute temperature, Range = 0 to 500 ℃

Nature of the hydrothermal water can be interpreted by the calculated oxygen isotopic composition of hydrothermal water, whether it is magmatic water origin, meteoric water origin, or seawater origin. Because it is known that the oxygen isotopic composition of magmatic water is +6‰ to +9‰ (Taylor, 1974), meteoric water is generally -4‰ to -14‰ with relation of $\delta D = 8 \delta\ ^{18}O + 10$ (Craig, 1963), and oceanic water is generally 0‰.

The oxygen isotopic compositions of hydrothermal water of epithermal Au veins in Japan, meteoric water, volcanogenic geothermal water and magmatic water are shown in Fig. 2 (MITI, 1999). It is understood that the volcanogenic geothermal water is formed by mixing of magmatic water and meteoric water, and hydrothermal water of epithermal Au veins are within a range of the volcanogenic geothermal water. Concerning the hydrothermal water of the Hishikari deposit that is famous for high grades of about 80g/t Au, shows the most wide range meaning the drastic mixing of magmatic water and meteoric water.

Fig. 2 $\delta^{18}O(‰)$ of water concerning ore forming fluids of epithermal Au veins and others. Data from Sakai and Matsubaya (1974), Taylor (1974), Hattori and Sakai (1979), Mizota and Kusakabe (1994) and MITI (1999).
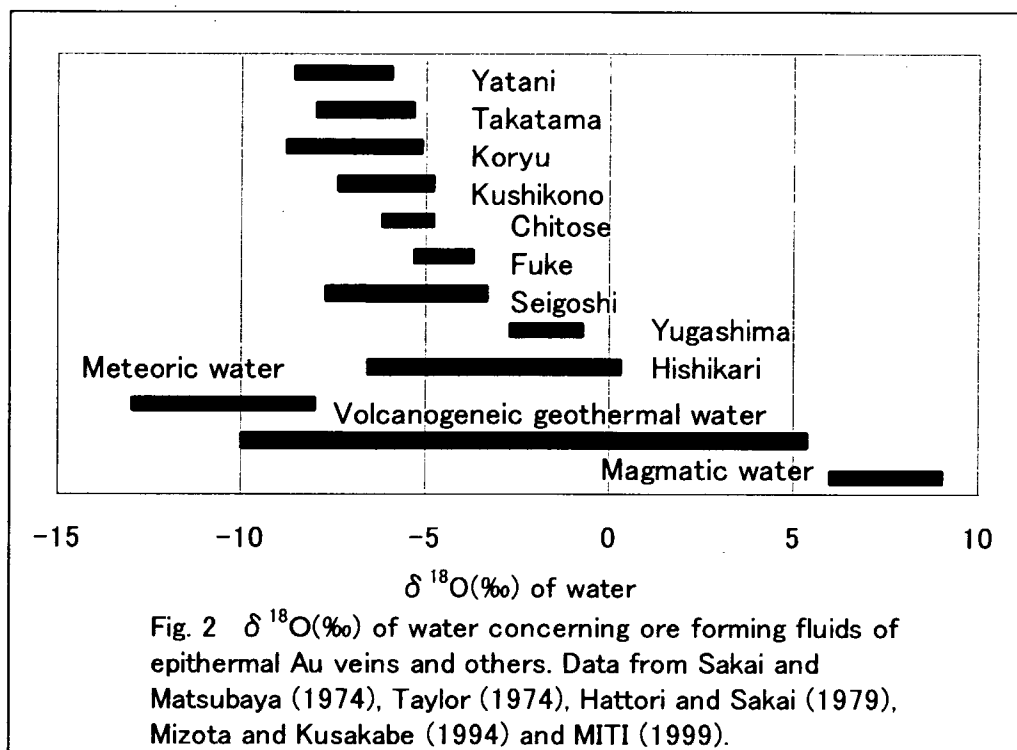
3. Rare earth elements (REE)

The spiderdiagram that is normalized pattern by the chondrite, primitive mantle, or MORB, are utilized to display the REE contents. REE are arranged on abscissa from left to right in increasing order of partition coefficient between ultramafic rock and basaltic magma.

Concerning granitiods, REE chondrite normalized pattern is generally utilized based on the recommended values for chondrite by Boynton (1984). Fig. 3 is a example of REE chondrite normalized patterns for granitoids of the Erdenet porphyry copper deposit area in Mongolia (JICA/MMAJ, 2000). In this case, La to Sm are called LREE (Light rare earth elements) and Gd to Lu are called HREE (Heavy rare earth elements). As shown in Fig. 3, the productive intrusions are depleted in REE than the barren intrusions, and significant depletions in HREE cause the productive intrusions steep right down profiles. Besides, the productive intrusions indicate the less negative or positive Eu anomalies. These characteristics are just concordant with the report of Lang and Titley (1998) concerning the REE chondrite normalized patterns to distinguish between productive and barren intrusions of the porphyry Cu deposits.
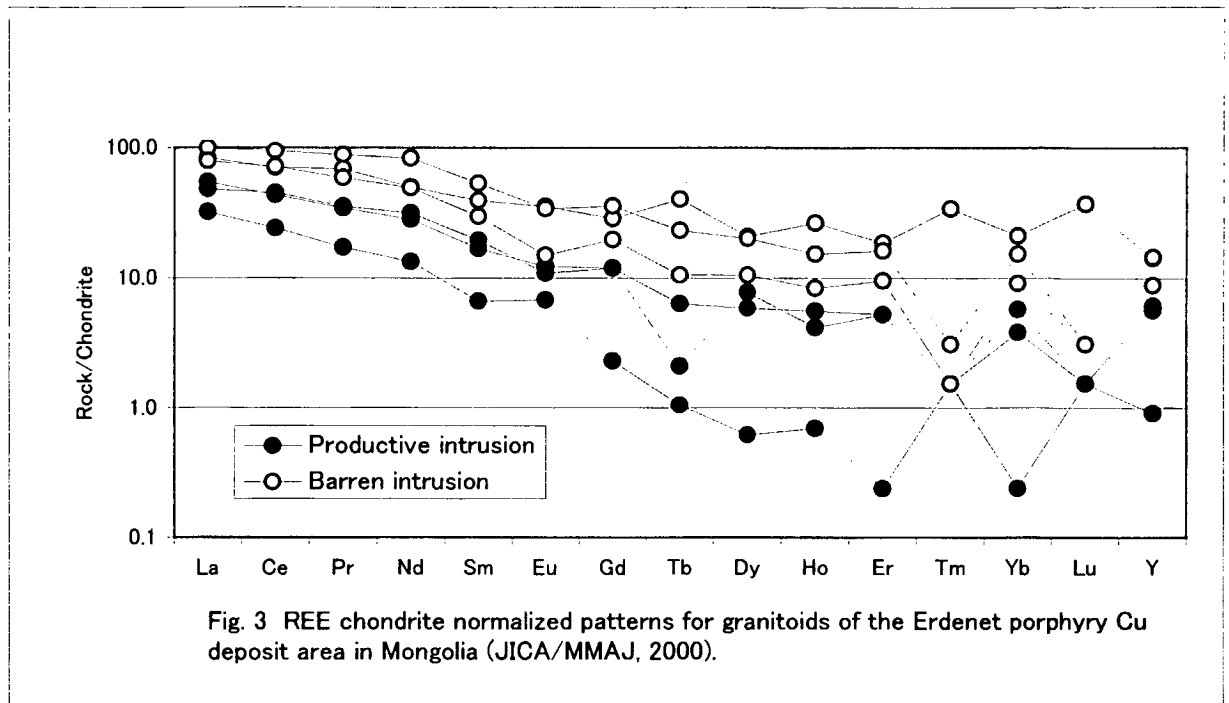
Fig. 3 REE chondrite normalized patterns for granitoids of the Erdenet porphyry Cu deposit area in Mongolia (JICA/MMAJ, 2000).

REE chondrite normalized patterns for minerals forming the granitoids are shown in Fig. 4. It is understood that REE is mainly contained in the minerals of allanite, sphene, zircon, apatite, hornblend and epidote, while plagioclase and K-feldspar lack HREE intensively and contain Eu selectively. Therefore, it is interpreted that early stage undifferentiated intrusion is enriched with REE because of the abundance of minerals
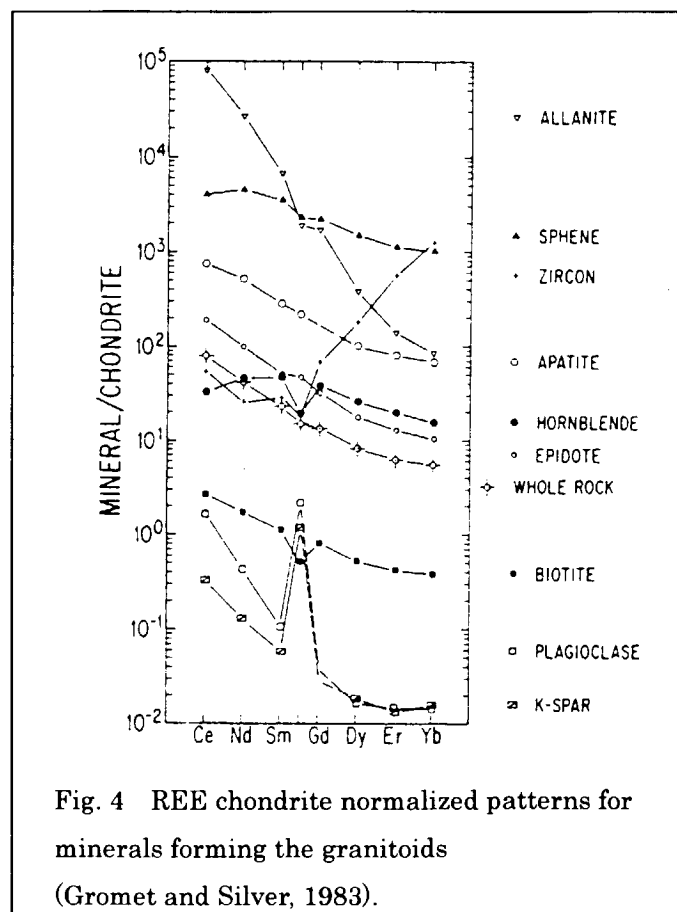
Fig. 4 REE chondrite normalized patterns for minerals forming the granitoids (Gromet and Silver, 1983).

rich in REE, while late stage differentiated intrusion is depleted with REE. Especially, if the differentiated intrusion is feldspathic, it may show intensive depletion of HREE and positive anomaly of Eu, same as the patterns of productive intrusions in the Erdenet area (Fig. 3).

Characteristics of the productive intrusions are simply displayed in chondrite normalized Ce/Yb vs Yb diagram, as Fig. 5 for case of the Erdenet area, because Ce/Yb cn (cn : chondrite normalized) represents the right down inclination of REE pattern in Fig. 3, and Yb cn represents the concentration of HREE. In Fig. 5, values of primitive mantle, MORB, continental crusts, A·type granite and tonalite – trondhjemite trend are also plotted with data of the Erdenet area. The productive intrusions are concordant with the differentiation of the tonalite – trondhjemite trend, and the barren intrusions are concordant with the undifferentiated continental crusts.

Fig. 5 REE chondrite normalized Ce/Yb – Yb diagram for granitoids of the Erdenet porphyry Cu deposit area in Mongolia.
cn : chondrite normalized, UC : upper continental crust, CC : continental crust, LC : lower continental crust, data except the Erdenet are from Ogasawara (1989).
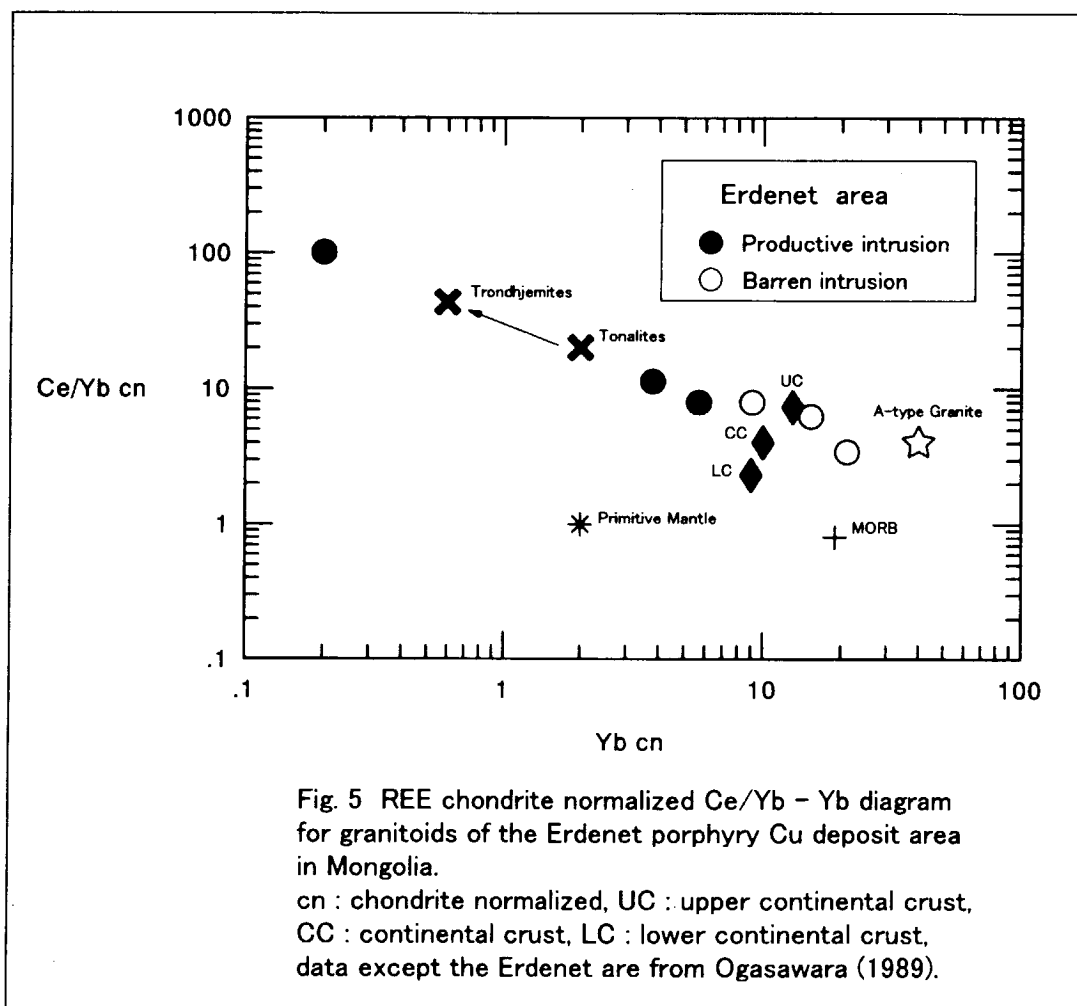
Meanwhile, Rb - Nb+Y diagram was developed by Pearce et al. (1984) for the tectonic setting discrimination (Fig. 6). Christiansen and Keith (1996) plotted the compositions of selected igneous rocks that are related to mineralization on diagram of Pearce (1984), after change of the field names to emphasize the granitoid types (Fig. 7A), and effect of various processes and source compositions are also shown on the diagram (Fig. 7B). Therefore, potentiality of mineralization can be implied by the plots of compositions on Rb – Nb+Y diagram.
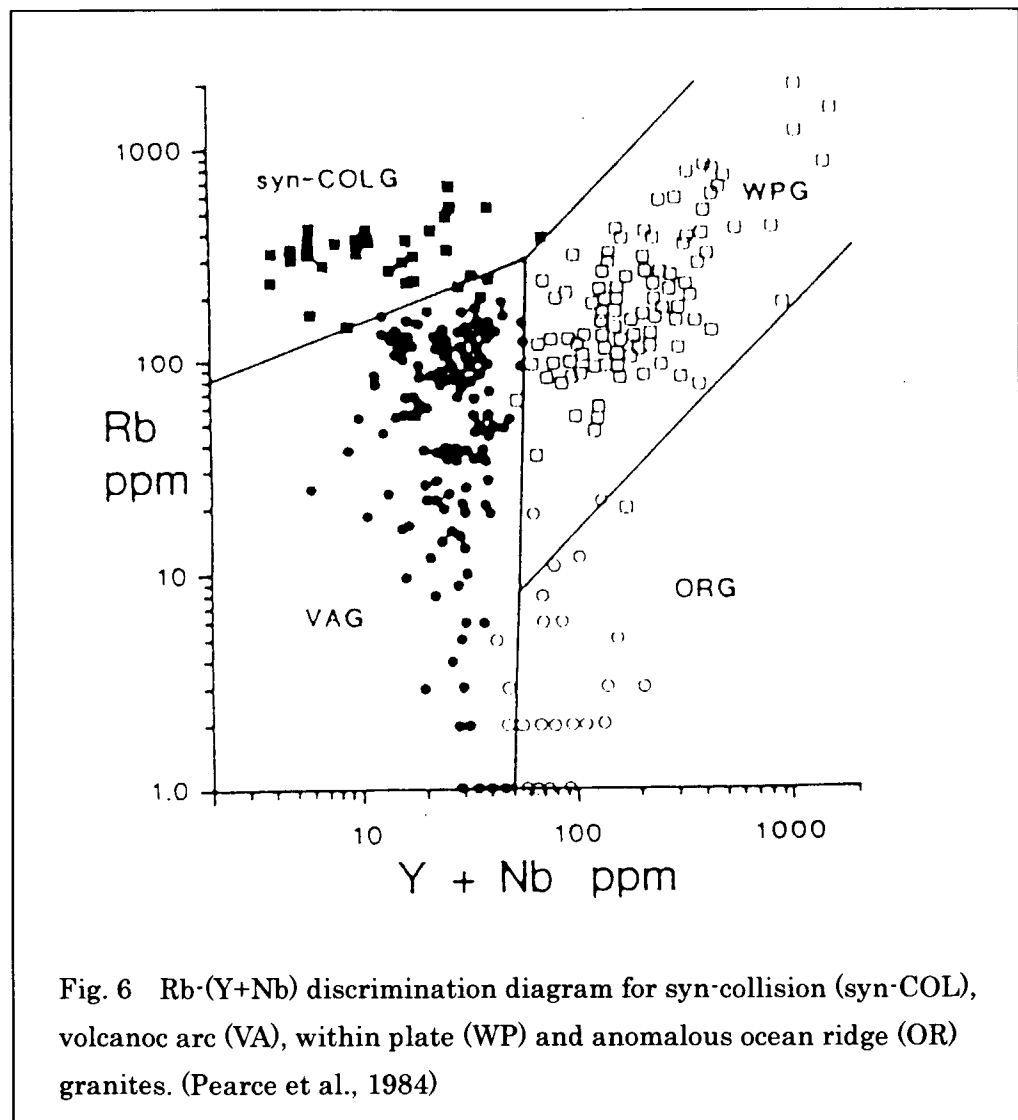
Fig. 6 Rb-(Y+Nb) discrimination diagram for syn-collision (syn-COL), volcanoc arc (VA), within plate (WP) and anomalous ocean ridge (OR) granites. (Pearce et al., 1984)
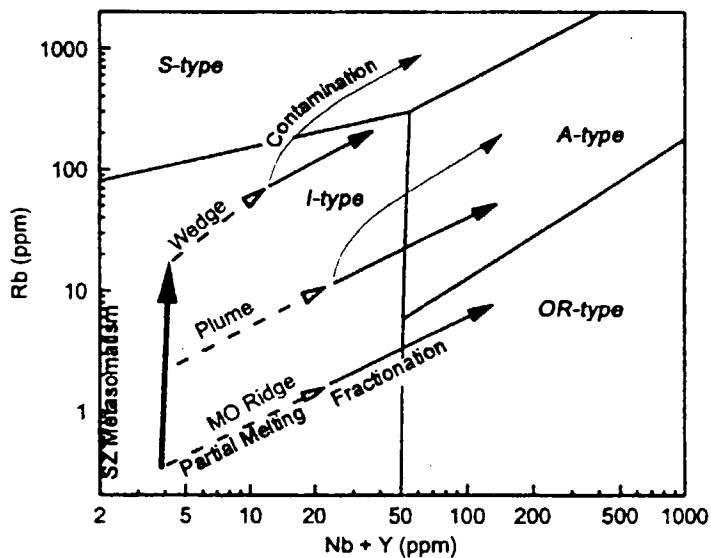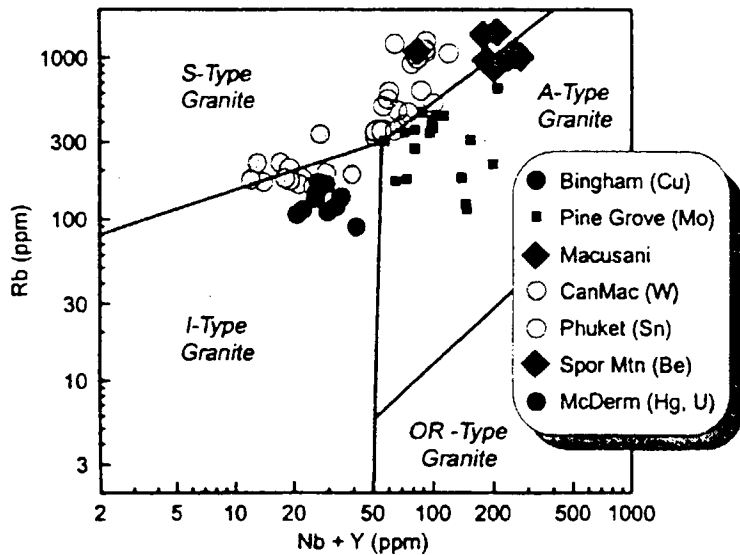
Fig. 7 (A) Upper: compositions of selected igneous rock suites that are related to mineralization plotted on Pearce et al. (1984) tectonic discrimination diagram. The field names have been changed to emphasize compositional, rather than, tectonic characteristics. (B) Lower: the effect processes and source compositions on trace element trends and positions on this diagram.

(Christiansen and Keith, 1996)

Appendix – 16

Plate 1 Villa Aguas Calientes district : A view of the alteration zone seen in the NW slope of Cerro La Puntilla

Plate 2 Villa Aguas Calientes district : Quartz vein in granitic rock along the lower stream of Atreuco creek

Plate 3 Villa Aguas Calientes district : Network of quartz veinlets in granitic rock
along the lower stream of Manchana Covunco creek

Plate 4 Varvarco district : A view of the white argillized and silicified zone along the
upper stream of Auquen creek

Plate 5 Varvarco district : A view of the no-named open pit located in the lower part of
a branch of Guaraco Norte creek

Plate 6 Varvarco district : A trench and drift entrance of Mina Santos located in the
upper stream of Guaraco Norte creek

Plate 7 Varvarco district : Ore samples of chalcopyrite-bearing pyrite quartz vein (left) and quartz vein with malachite and azulite (right), collected in the stock pile of Mina Santos
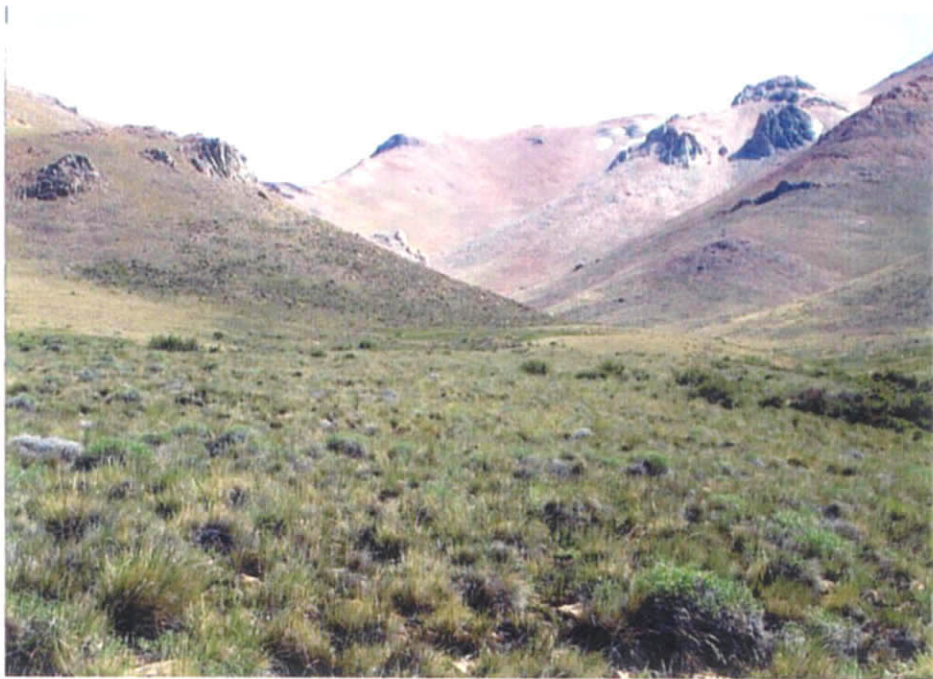
Plate 8 Cerro Collocho district : A view of the alteration zone of the Cerro Collocho

Plate 9 Cerro Collocho district : A zone of limonite (after pyrite) -quartz vein in the
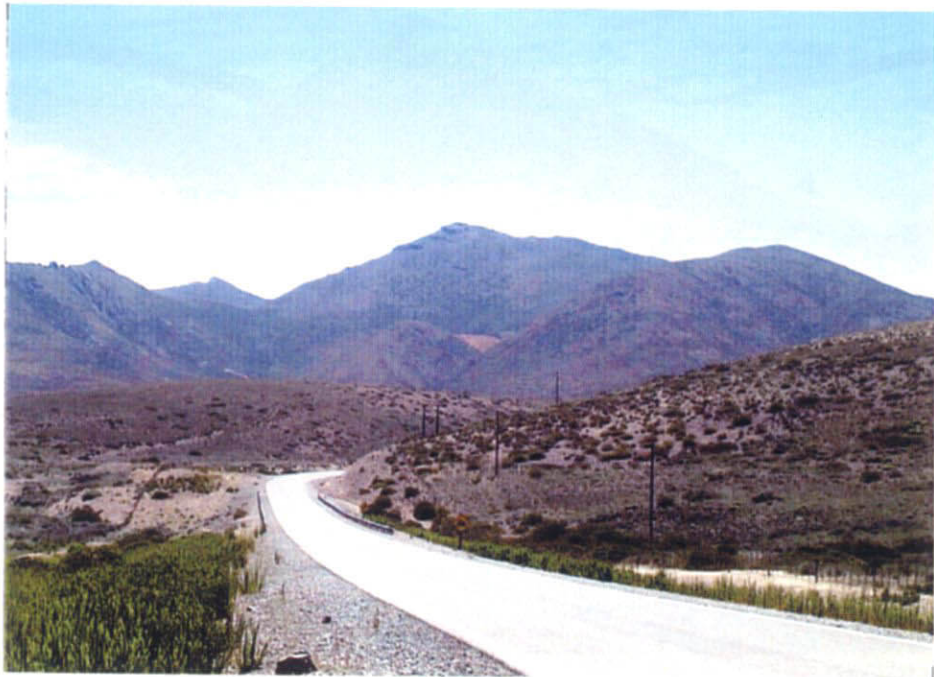silicified dacitic andesite

Plate 10 Cerro Mayal district : A view of Cerro de Mayal Mahuida, argillic alteration
seen on the middle slope of the mountain

Plate 11 Cerro Mayal district : An old trench located near the peak of the mountain

Plate 12 Cerro Mayal district : A view of the alteration zone located on a small ridge in
the eastern side of the mountain

Plate 13 Cerro Mayal district : Float rocks with malachite along crack

Plate 14 Cerro de los Bueyes district : A view of Cerro de los Bueyes. The bedded
sedimentary rocks around the central peak is widely altered.

Plate 15 Cerro de los Bueyes district : A view of white argillic alteration near the top of
the mountain

Plate 16 Cerro de los Bueyes district : An outcrop of bedded mineralized sandstone and
shale. The sandstone is selectively replaced by marcasite and quartz

Plate 17 Cerro de los Bueyes district : A view of Cerro los Potreritos with an alteration
zone on the top of and behind the mountain

Plate 18 Campana Mahuida district : A view of the Pino Andino prospect area

Plate 19 Campana Mahuida district : An outcrop of the hydrothermal breccia

Plate 20 Campana Mahuida district : Macroscopic view of a hydrothemal breccia with
　　　　large quartz crystals

Plate 21 Campana Mahuida district : A short trench with a stock pile of barite ore with
malachite

Plate 22 Campana Mahuida district : Thick Quaternary sediments in the West side of
the Pino Andino prospect area

Plate 23 Palau Mahuida district : A silicified and argillized zone. In the far right side,
pyrite-limonite are disseminated in yellow-brown zone. In the near side, gray
colored andesite porphyry is fresh (ZA007).

Plate 24 Palau Mahuida district : An outcrop of silicified and argillized rock with pyrite
or limonite dissemination (ZA007).

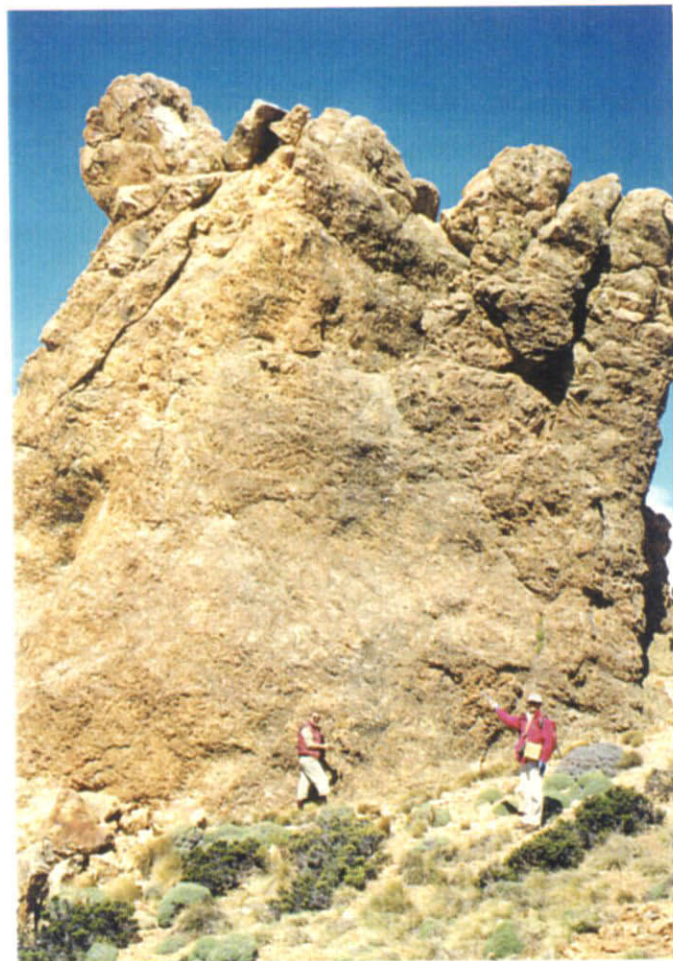Plate 25 Nireco district : An outcrop of silicified and argillized rhyolite with limonite or jarosite dissemination (ZA007).

Plate 26 Nireco district : A steeple like silicified and argillized rhyolite with flow band (ZA023).

Plate 27 La Voluntad district : An outcrop of hydrothermal breccia which crosscuts silicified and argillized banded rhyolite (ZA032).

Plate 28 La Voluntad district : An outcrop of silicified and argillized banded rhyolite (ZA032).

Plate 29 Rio Foyel district : A quartz vein hosted in weakly altered granitoid (SB068).

Plate 30 Rio Foyel district : A silicified and argillized zone distributed around the ridge
of Cerro Carrera. A dark colored zone in the center is a fresh basalt dyke
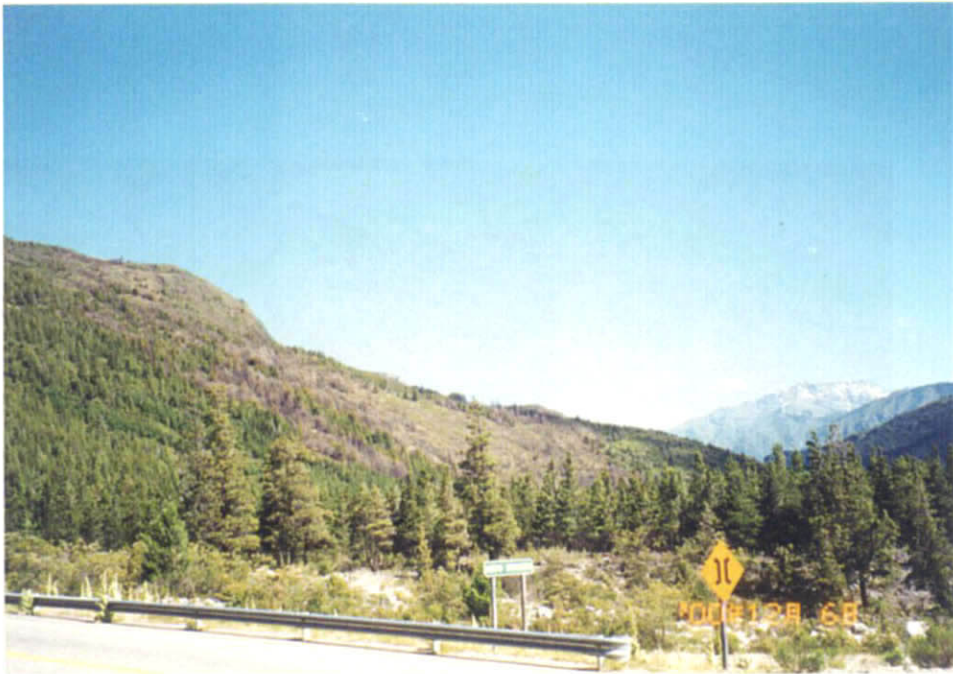(SB068).

Plate 31 Condorcanqui district : A distant view of the Condorcanqui district from No. 258 National road.

Plate 32 Condorcanqui district : Large outcrop of andesite lava in the upper stream of Arroyo Buen Sonido. K-Ar radiometric dating revealed 28.1±1.4 Ma.

Plate 33 Condorcanqui district : Post-mineralization andesite dyke in the host rock andesite of malachite. K-Ar radiometric dating of dyke revealed 108±5 Ma.

Plate 34 Epuyén district : A distant view of Cordón de Cholila from south.

Plate 35 Epuyén district : Reddish brown colored mineralized outcrop along Rio Blanco.
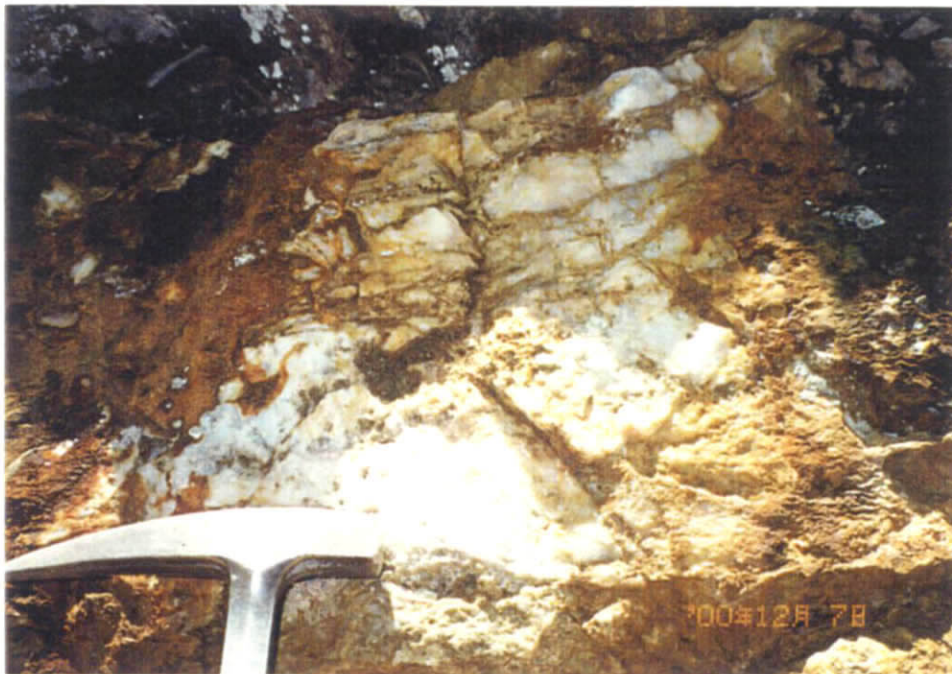Host rock is quartz porphyry.

Plate 36 Epuyén district : Quartz vein with limonite in the mineralized outcrop of
Plate 35. Chemical analysis revealed 9.14g/t Au.

Plate 37 Epuyén district : White quartz vein of 1m width at Epuén lakeside. Host rock is silicified sandstone of Jurassic.

Plate 38 Laguna Sunica district : A distant view of alteration zones of Laguna Sunica from northwest.

Plate 39 Laguna Sunica district : Zeolite veinlets network in altered basalt of the
Ventana formation of Paleogene.

Plate 40 Cerro Gonzalo district : A distant view of Sector 2 to Sector 6 from northeast.
Sector 2 is prominent outcrop in left side. Sector 6 is on high land of right side.

Plate 41 Cerro Gonzalo district : A view of Sector 1 (Arroyo Luque) from southwest. Hypogen porohyry Cu deposit exposes along the river.

Plate 42 Cerro Gonzalo district : Reddish limonitic zone on a hill of Sector 1 (Arroyo Luque). Malachite is partially observed.
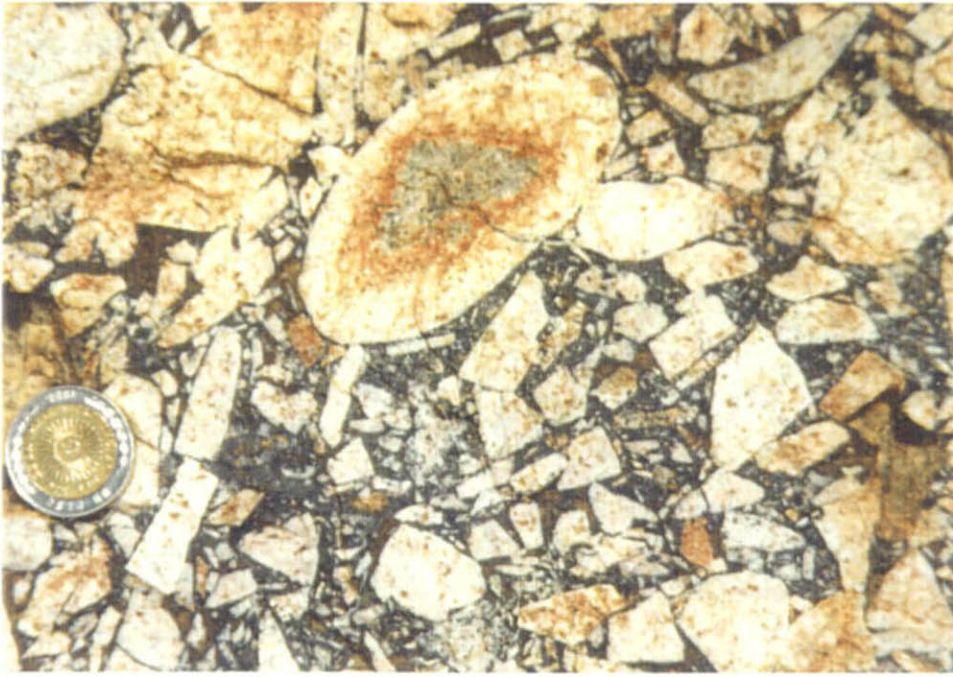
Plate 43 Cerro Gonzalo district : Hydrothermal breccia in Sector 3. Matrix part is filled
with black tourmaline of fine size.

Plate 44 Arroyo Cascada district : A distant view of Arroyo Cascada from east.

Plate 45 Arroyo Cascada district : Quartz veins of relative flat structure in silicified andesite of Jurassic. 4.07g/t Au was revealed.

Plate 46 Arroyo Cascada district : Quartz veinlets network in microdiorite in the southeast part of alteration zone.

Plate 47 Cerro Cuche district : A view of steep slopes with alteration zones from south.

Plate 48 Cerro Cuche district : A view of alteration zones in lower part. It is seen from
northern higher point.